RANKING THE VEGETATION INDICES FOR MACHINE LEARNING SPECIFIC TASKS

Serban OPRISESCU[1], Mihai IVANOVICI[2], Corneliu FLOREA[3]

Vegetation indices are useful tools in smart agriculture for many applications such as assessment of plant health, estimation of yield, drought prediction. This study examines the measure in which each of these specialized vegetation indices contributes to crop discrimination in a classification process. We begin with a correlation study of 36 vegetation indices computed on PRISMA hyperspectral images. Then we propose an algorithm based on principal components for the removal of redundant vegetation indices, while the efficiency is measured over the resulting images with structural similarity. Finally, a comparison is made in terms of segmentation results using Random Forests, ResNet, U-Net and SE-ResNet on the whole hyperspectral image vs. a multiband selected vegetation indices image. Our results show that the proposed vegetation index selection method is effective for hyperspectral image segmentation

Keywords: Agriculture, vegetation indices (VIs), correlation matrix, Principal Component Analysis (PCA), Random Forests (RF), hyperspectral image segmentation

1. Introduction

The hyperspectral optical satellites such as PRISMA (Hyperspectral Precursor of the Application Mission) owned by the Italian Space Agency (ASI) offer a high spectral resolution in the visible, near and short-wave infrared spectrum. This capability opens the way to numerous remote sensing applications that can more precisely characterize the development stage and health of agricultural crops. Among many examples, agriculture benefits from the hyperspectral imaging (HSI) [1] for a better land use characterization (crop identification and monitoring), crop health monitoring (drought or disease detection, plant stress detection), yield estimation etc.

Vegetation indices (VIs) are widely used for remote sensing applications [2]. Most of these indices take the form of a ratio between linear combinations of different spectral bands and are specially designed to assess vegetation cover, health

[1]* Lecturer within the Electronics and Computers Department, Transilvania University of Brașov, Romania, corresponding author (e-mail: serban.oprisescu@unitbv.ro)
[2] Professor, Electronics and Computers Department, Transilvania University of Brașov, Romania (e-mail: mihai.ivanovici@unitbv.ro)
[3] Professor, National University of Science and Technology POLITEHNICA of Bucharest, Romania (e-mail: corneliu.florea@upb.ro)

and growth [2]. Many works have studied the correlation between some chosen VIs and different plant characteristics measured in situ such as vigor, leaf coverage area, growth, some specific diseases etc. [2]. These studies show that many VIs are very useful in characterizing plant physiology and growth.

Given the amount of VIs, there is the practical question whether they identify new information, or they are highly redundant. There are several works that investigate this aspect. For instance, a „significant" correlation between NDVI and LAI has been found [3] due to the fact that LAI was found to be strongly correlated with the NIR band. In addition, it also states that LAI is linearly related to EVI, with a correlation coefficient of 0.77. In [4] the correlations between several spectral bands are highlighted, for instance between the red and blue bands (R2=0.96) of Moderate Resolution Imaging Spectroradiometers (MODIS); thus, in [4] a 2-band EVI (EVI2) vegetation index has been proposed. Hill [5] studied the magnitude of correlation matrices between five vegetation indices for six different regions from the USA. He notices some common trends between all the six regions and observes some variations of the correlation coefficient values.

In this paper we propose a methodology for the elimination of redundant VIs from a similarity perspective. We start with an initial set of 36 VIs and we eliminate one-by-one each VI by taking into account the correlation matrix and the structural similarity index measure (SSIM) computed on the first component of the PCA of the VIs set. The resulting set of less-correlated VIs is used as input for a random forest segmentation and compared, in terms of accuracy, with a random forest segmentation directly applied on the 187-band hyperspectral satellite image. ResNet, U-Net and SE-ResNet CNNs are also used for comparison.

2. Vegetation Indices Correlation Study

There are more than 100 vegetation indices documented in various remote sensing papers [2]. The starting point of our study was the observation that many of these VIs have very similar equations. For instance, the well-known NDVI = (NIR – Red) / (NIR + Red) (Normalized Difference Vegetation Index) and SAVI = ((NIR – Red) / (NIR + Red + L)) . (1 + L) (Soil-Adjusted Vegetation Index).
where L represents the vegetation cover and takes values between 0 and 1; in areas with moderate vegetation cover L=0.5, value taken in this study.

Considering this observation, but also the fact that many vegetation indices are computed using the same spectral bands, high degrees of correlations are expected to be found on the images obtained from these indices.

For the first part of this study, after talking to an agricultural engineer, we decided to use 36 VIs, which are the ones presented in Table I. The denominations of these indices are the following: Normalized Difference Vegetation Index - NDVI, Anthocyanin Reflectance Index - ARI, Modified Anthocyanin Reflectance

Index - ARI2, Atmospherically-Resistant Vegetation Index - ARVI, Enhanced Vegetation Index - EVI, Green Atmospherically Resistant Index - GARI, Green Normalized Difference Vegetation Index - GNDVI, Green Vegetation Index - GVI, Infrared Percentage Vegetation Index - IPVI, Leaf Area Index - LAI, Modified Non-Linear Index - MNLI, Modified Simple Ratio - MSR, Non-Linear Index - NLI, Optimized Soil Adjusted Vegetation Index - OSAVI, Renormalized Difference Vegetation Index - RDVI, Soil Adjusted Vegetation Index - SAVI, Simple Ratio - SR, Transformed Difference Vegetation Index - TDVI, Visible Atmospherically Resistant Index - VARI, Modified Chlorophyll Absorption Ratio Index - MCARI, Modified Chlorophyll Absorption Ratio Index 2 - MCARI2, Modified Triangular Vegetation Index 1 - MTVI1, Modified Triangular Vegetation Index 2 - MTVI2, Transformed Chlorophyll Absorption Ratio - TCARI, Triangular Vegetation Index - TVI, Vogelmann Red Edge Index 1 - VREI1, Vogelmann Red Edge Index 2 - VREI2, Plant Senescence Reflectance Index - PSRI, Normalized Difference Infrared Index - NDII, Carotenoid Reflectance Index 2 - CRI2, Difference Vegetation Index - DVI, Normalized Difference Nitrogen Index - NDNI, Moisture Stress Index - MSI, Normalized Multi-band Drought Index - NMDI, Water Band Index - WBI and Photochemical Reflectance Index - PRI. References for all these indices can be found in [6].

Table 1

The 36 vegetation indices used

Nb.	Acronym	Description	Equation	Wavelengths (nm)
1	NDVI	Norm. Difference Vegetation Index	$NDVI = (NIR\text{-}Red)/(NIR+Red)$	684.1, 806.7
2	ARI	Anthocyanin Reflectance Index	$ARI1 = 1/\rho_{550} - 1/\rho_{700}$	550.9, 703.7
3	ARI2	Modified Anthocyanin Reflectance Index	$ARI2 = \rho_{800}\left[\frac{1}{\rho_{550}} - \frac{1}{\rho_{700}}\right]$	806.7, 550.9, 703.7
4	ARVI	Atmosph.-Res. Vegetation Index	$ARVI = \frac{NIR - [Red - \gamma(Blue - Red)]}{NIR + [Red - \gamma(Blue - Red)]}$	453.4, 684.1, 806.7
5	EVI	Enhanced Vegetation Index	$EVI = 2.5\frac{(NIR-Red)}{(NIR+6*Red-7.5*Blue+1)}$	453.4, 684.1, 806.7
6	GARI	Green Atm. Resistant Index	$GARI = \frac{NIR - [Green - \gamma(Blue - Red)]}{NIR + [Green - \gamma(Blue - Red)]}$ $\gamma = 1.7$	453.4, 559, 684.1, 806.7
7	GNDVI	Green Norm. Diff. Veg. Index	$GNDVI = (NIR\text{-}Green)/(NIR+Green)$	550.9, 754.5
8	GVI	Green Vegetation Index	$GVI = (-0.2848TM_1) + (-0.2435TM_2) + (-0.5436TM_3) + (0.7243TM_4) + (0.084TM_5) + (-0.18TM_7)$	482.5, 559, 664.9, 827.9, 1647, 2215

9	IPVI	Infrared Percent. Veg. Index	$IPVI = NIR/(NIR+Red)$	684.1, 806.7
10	LAI	Leaf Area Index	$LAI = (3.618 * EVI - 0.118) > 0$	453.4, 684.1, 806.7
11	MNLI	Modified Non-Linear Index	$MNLI = \frac{(NIR^2 - Red) * (1+L)}{NIR^2 + Red + L}$	684.1, 806.7
12	MSR	Modified Simple Ratio	$MSR = (NIR/Red - 1) / \left(\sqrt{NIR/Red} + 1\right)$	684.1, 806.7
13	NLI	Non-Linear Index	$NLI = (NIR^2 - Red)/(NIR^2 + Red)$	703.7, 944.6
14	OSAVI	Opt. Soil Adj. Veg. Index	$OSAVI = \frac{1.5 * (NIR - Red)}{(NIR + Red + 0.16)}$	664.9, 806.7
15	RDVI	Renorm. Diff. Vegetation Index	$RDVI = \frac{(NIR - Red)}{\sqrt{(NIR + Red)}}$	684.1, 806.7
16	SAVI	Soil Adjusted Vegetation Index	$SAVI = \frac{1.5 * (NIR - Red)}{(NIR + Red + 0.5)}$	684.1, 806.7
17	SR	Simple Ratio	$SR = NIR / Red$	684.1, 806.7
18	TDVI	Transf. Diff. Vegetation Index	$TDVI = \sqrt{0.5 + \frac{(NIR - Red)}{(NIR + Red)}}$	684.1, 806.7
19	VARI	Visible Atmosph. Resistant Index	$VARI = \frac{Green - Red}{Green + Red - Blue}$	475.3, 550.9, 655.4
20	MCARI	Mod. Chlorophyll Abs. Ratio Index	$MCARI = [(\rho_{700} - \rho_{670}) - 0.2(\rho_{700} - \rho_{550})] * (\rho_{700}/\rho_{670})$	542.9, 664.9, 703.7
21	MCARI2	Mod. Chlorophyll Abs. Ratio Ind. 2	$MCARI2 = \frac{1.5[2.5(\rho_{800} - \rho_{670}) - 1.3(\rho_{800} - \rho_{550})]}{\sqrt{(2\rho_{800}+1)^2 - (6\rho_{800} - 5\sqrt{\rho_{670}}) - 0.5}}$	542.9, 664.9, 806.7
22	MTVI1	Mod. Triangular Veg. Index 1	$MTVI = 1.2[1.2(\rho_{800} - \rho_{550}) - 2.5(\rho_{670} - \rho_{550})]$	542.9, 664.9, 806.7
23	MTVI2	Mod. Triangular Veg. Index 2	$MTVI2 = \frac{1.5[1.2(\rho_{800} - \rho_{550}) - 2.5(\rho_{670} - \rho_{550})]}{\sqrt{(2\rho_{800}+1)^2 - (6\rho_{800} - 5\sqrt{\rho_{670}}) - 0.5}}$	542.9, 664.9, 806.7
24	TCARI	Transf. Chloroph. Abs. Ratio	$TCARI = 3\left[(\rho_{700} - \rho_{670}) - 0.2(\rho_{700} - \rho_{550})\left(\frac{\rho_{700}}{\rho_{670}}\right)\right]$	542.9, 664.9, 703.7
25	TVI	Triangular Vegetation Index	$TVI = 0.5[120(\rho_{750} - \rho_{550}) - 200(\rho_{670} - \rho_{550})]$	550.9, 674.5, 754.4
26	VREI1	Vogelmann Red Edge Index 1	$VREI1 = \rho_{740} - \rho_{720}$	723.9, 744.1
27	VREI2	Vogelmann Red Edge Index 2	$VREI2 = \frac{\rho_{734} - \rho_{747}}{\rho_{715} + \rho_{726}}$	713.7, 723.9, 733.9, 744.1
28	PSRI	Plant Senescence Ref. Index - PSRI	$PSRI = \frac{\rho_{680} - \rho_{500}}{\rho_{750}}$	497, 684.1, 754.5
29	NDII	Norm. Difference Infrared Index	$NDII = \frac{(\rho_{819} - \rho_{1649})}{(\rho_{819} + \rho_{1649})}$	817.3, 1647
30	CRI2	Carotenoid Refl. Index 2	$CRI2 = \frac{1}{\rho_{510}} - \frac{1}{\rho_{700}}$	512, 703.7
31	DVI	Difference	$DVI = NIR - Red$	684.1, 806.7

		Vegetation Index		
32	NDNI	Norm. Difference Nitrogen Index	$NDNI = \frac{\log(1/\rho_{1510}) - \log(1/\rho_{1680})}{\log(1/\rho_{1510}) + \log(1/\rho_{1680})}$	1512.6, 1677.3
33	MSI	Moisture Stress Index	$MSI = \rho_{1599}/\rho_{819}$	817.3, 1596.2
34	NMDI	Norm. M.-band Drought Ind.	$NMDI = \frac{\rho_{860} - (\rho_{1640} - \rho_{2130})}{\rho_{860} + (\rho_{1640} - \rho_{2130})}$	860, 1596.2, 2127.3
35	WBI	Water Band Index	$WBI = \rho_{970}/\rho_{900}$	967, 902.8
36	PRI	Photochemical Reflectance Index	$PRI = \frac{\rho_{531} - \rho_{570}}{\rho_{531} + \rho_{570}}$	527.3, 567.2

For our experiments we used PRISMA hyperspectral images of the area of Brasov city, Romania. More precisely we used Level 2c images which contain at-surface reflectance - atmospherically corrected values [7]. Each image contains 187 spectral bands (after we removed water-absorption bands) in the wavelength interval [400nm, 2500nm]. The spectral resolution is higher than 12nm. The spatial resolution is 30m (each image has 1000x1000 pixels and represents an area of 30x30km on the ground). In Fig. 1 a band selection visualization of a PRISMA image from Brasov region, acquired on 24 Mars 2023 is shown.

Fig. 1. RGB band selection of a PRISMA image from 24 Mars 2023, Brasov region, Romania.

We calculated each vegetation index from Table I using the formulas from the literature. The high spectral resolution of the PRISMA Hyperspectral Imager allowed us to precisely compute these VIs using their equations. For instance, in the case of GNDVI = (NIR – Green) / (NIR + Green), in [8] has been proposed for NIR the wavelength of 750nm and for Green 550nm. To compute GNDVI in our algorithm, we chose the 754.5nm and the 550.9nm bands, which are very close to the theoretical wavelengths.

In the first part of this study, we computed the correlation matrix for all the 36 chosen VIs, having as input data several PRISMA images from the Brasov region. Fig. 2 shows such a correlation matrix obtained from the hyperspectral image visualized in Fig. 1. Each number written on the axis of Fig. 2 represents the vegetation index from Table I.

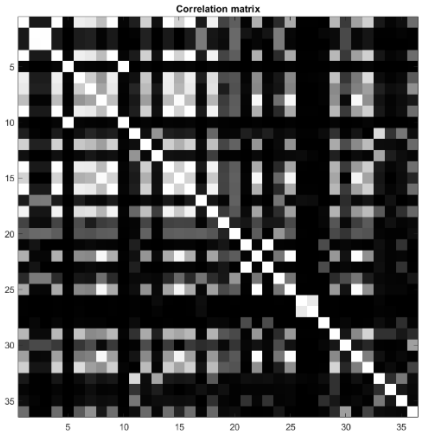

Fig. 2. Correlation matrix for all the 36 VIs computed on the hyperspectral image visualized in Fig. 1.

The aspect of the correlation matrix remains the same (with slight variations) when the input data represents a PRISMA image of the same location, but from different dates: 24.03.2023, 19.06.2024 and 30.06.2024. This shows that at least on the specific land cover (spring and summer) of the Brasov area, the correlations between VIs stays the same. Table II contains 15 lines with the most correlated VIs obtained on the image from Fig. 1.

Having strong correlations between the 36 chosen VIs, there is the need for a methodology to reduce the number of VIs only to the relevant (from the perspective of a specific task, like a Machine Learning - based classification or segmentation), less correlated ones. One idea was to keep only the dark lines from the correlation matrix (Fig. 2), which signals the uncorrelated values.

In the second part of this study, we propose an alternative, which is an algorithm that eliminates the redundant, strong correlated VIs, based on the structural similarity index measure (SSIM) [9]. The motivation lies in the fact that originally VIs have been introduced for the emphasis of certain aspects of interest. SSIM is built to identify regions that are visually and structurally similar.

Table 2
The Most Correlated Vegetation Indices

VI #1	***VI #2***	***r***
IPVI	NDVI	1.0000
LAI	EVI	1.0000
MTVI2	MCARI2	1.0000

SAVI	NDVI	1.0000
SAVI	IPVI	1.0000
ARVI	NDVI	0.9992
IPVI	ARVI	0.9992
SAVI	ARVI	0.9992
TVI	MTVI1	0.9964
OSAVI	NDVI	0.9957
OSAVI	IPVI	0.9957
SAVI	OSAVI	0.9957
ARI2	ARI	0.9950
OSAVI	ARVI	0.9945
DVI	MTVI1	0.9903

The proposed redundant VIs elimination algorithm (Alg. 1) starts with PCA computed on the entire 36 VIs image volume. The resulting first component contains the most information (has the largest variation), and this is why only the first component is used in this algorithm. At each step of the algorithm only one vegetation index is removed – in the decreasing order of correlation with the other VIs (by looking at the correlation matrix). After removal, the first component of PCA applied on the VIs image volume with the removed index (denoted ALL_VI_i) is calculated. Then this value, denoted P_i in Algorithm 1, is compared with the initial first component P_1, using SSIM. The result of the algorithm is an array of SSIM values with decreased magnitudes (the images are less and less similar to the initial first component P_1). Fig. 3 shows this variation of the SSIM value after the removal of each vegetation index. In Table III the SSIM value after the removal of each VI is recorded. One notices a dramatic decrease of SSIM after the removal of the Triangular Vegetation Index (TVI) from 1 to 0.044. The next decrease is after the removal of the Transformed Difference Vegetation Index (TDVI), from 0.044 to -0.08.

Alg. 1 Eliminating VIs

compute the 36 VIs
  denote ALL_VI the 36 VIs image volume
  compute PCA(ALL_VI)
  denote P_1 = first component of PCA(ALL_VI)
  for *i* = 1,…,35
    remove the least correlated vegetation index
    denote ALL_VI_i the image volume with the removed index
    compute P_i = the first component of PCA(ALL_VI_i)
    compute SSIM(P_1, P_i)

Fig. 4 a) shows a RGB representation of the three components of PCA (R = first, G = second, B = third component) when the PCA is computed on the VIs

image stack. Fig. 4 b) shows the result obtained with the PCA computed on the 187-band image. One notices the reddish color of the Fig. 4 a) which shows that the first component of PCA is much higher than the 2nd and the 3rd components. This means that the PCA is able to better compress the VI image / data with respect to the raw data. This analysis allowed us to conclude that we can remove the first 9 VIs that have the SSIM value equal to one in Fig. 3, because they are redundant, and keep only 27 VIs. One notices that each one of the nine removed VIs have a very strong correlation with one or more VIs from the 27 left.

3. Hyperspectral Image Segmentation

The third part our study focuses on the segmentation of the PRISMA hyperspectral image. The purpose of the segmentation is to distinguish between several types of agriculture crops. As segmentation algorithm we chose random forests (RF) [10]. The following five classes have been selected: rapeseed, winter wheat, built-up areas, bare soil and forest, representative both to the studied area (agricultural crops, city, mountains) and to the moment of the image acquisition (March). For training we used five corresponding patches of around 15x15 pixels. Fig. 5 a) shows a PRISMA image crop of 400x400 pixels; the five training areas are colored and numbered.

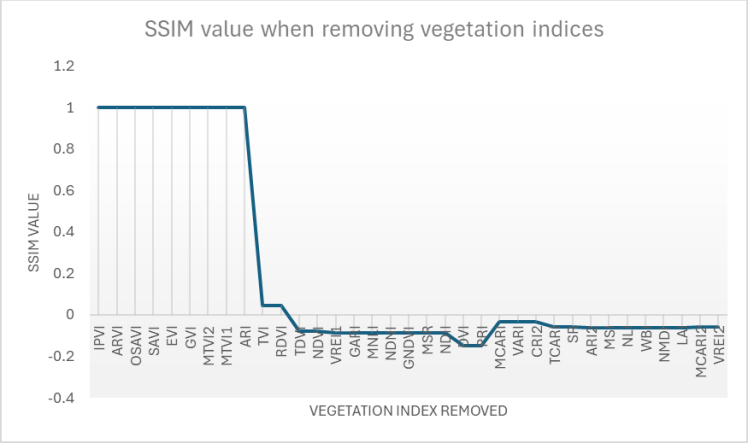

Fig. 3. SSIM value when removing vegetation indices.

Table 3

The SSIM value after removal of each VI

#	1	2	3	4	5	6	7	8	9	10	11	12
VI name	IPVI	ARVI	OSAVI	SAVI	EVI	GVI	MTVI2	MTVI1	ARI	TVI	RDVI	TDVI

SSIM value	1	1	1	1	1	1	1	1	1	0.044	0.044	-0.08
#	13	14	15	16	17	18	19	20	21	22	23	24
VI name	NDVI	VREI1	GARI	MNLI	NDNI	GNDVI	MSR	NDII	DVI	PRI	MCARI	VARI
SSIM value	-0.08	-0.085	-0.085	-0.085	-0.085	-0.085	-0.085	-0.085	-0.149	-0.149	-0.035	-0.035
#	25	26	27	28	29	30	31	32	33	34	35	
VI name	CRI2	TCARI	SR	ARI2	MSI	NLI	WBI	NMDI	LAI	MCARI2	VREI2	
SSIM value	-0.034	-0.059	-0.059	-0.061	-0.061	-0.061	-0.061	-0.061	-0.061	-0.059	-0.059	

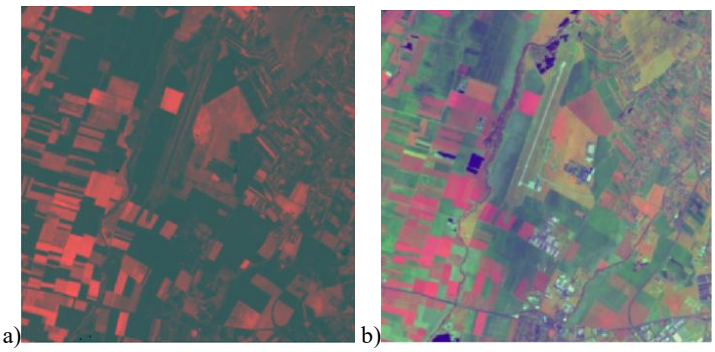

Fig. 4. a) first three components of PCA(VIs); b) first three components of PCA(187 bands image)

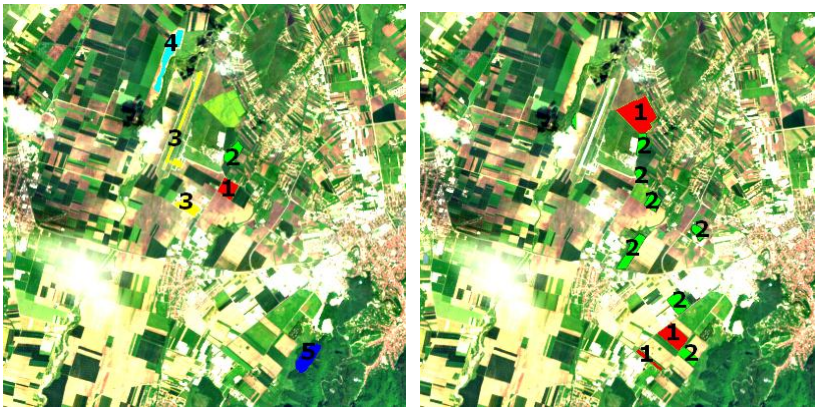

Fig. 5. a) The image crop with labeled training areas (1. rapeseed – red, 2. winter wheat – green, 3. built-up areas – yellow, 4. bare soil – cyan, 5. forest – blue). b) The image crop with labeled test areas (1. rapeseed – red, 2. wheat – green).

Fig. 6 a) shows the result of the segmentation when the input data for the RF algorithm consists of all the 187 spectral bands. Fig. 6 b) shows the segmentation result when the input data is represented by the 27 VIs previously selected in the second part of our experiment. For both results the same training areas as in Fig. 5 a) were used. One notices that in Fig. 6 b) a more precise differentiation between vegetation and non-vegetation areas is obtained, due to the specialization of the VIs to characterize vegetation.

Table III presents the obtained segmentation accuracy for both cases (Fig. 6 a) and Fig. 6 b)). As quality measures we used the border error (BE) [11], Jaccard index, rand index (RI or accuracy) and the F1 score. The BE should be ideally zero and is computed using (4), where A represents the segmented area and M is the reference area from the ground truth.

$$BE = Area((A \cup M) - Area(A \cap M))/Area(M) \quad (4)$$

In recent years, deep learning techniques have been increasingly adopted for hyperspectral image segmentation and classification, with numerous well-established backbone architectures demonstrating strong performance. These include autoencoders (AEs), convolutional neural networks (CNNs), recurrent neural networks (RNNs), generative adversarial networks (GANs), capsule networks (CapsNets), and graph convolutional networks (GCNs) [12]. Hong et al. [12] proposed SpectralFormer, one of the first Transformer-based architectures specifically designed for hyperspectral image classification, demonstrating that spectral self-attention can effectively model long-range spectral dependencies and outperform conventional CNN-based approaches. Sun et al. [13] introduced the Spectral–Spatial Feature Tokenization Transformer (SSFTT), which jointly exploits spectral and spatial information by tokenizing spectral–spatial features and modeling their long-range dependencies through self-attention for hyperspectral image classification. Ahmad et al. [14] proposed DiffFormer, a Differential Spatial Spectral Transformer that introduces a differential multi head self-attention mechanism and spectral spatial tokenization to enhance feature discrimination and classification accuracy for hyperspectral image classification, demonstrating superior performance and efficiency over prior state of the art models.

We repeated the segmentation experiments using the same training and test regions but changing the segmentation method. We defined a custom 1D Residual Network (ResNet) architecture which takes as input a single hyperspectral / multiband pixel. The network begins with an initial convolutional block that acts as a feature extractor. Following this, the core of the network consists of two residual blocks, each comprising a main path of two convolutional layers (having kernels of size [5 1]), batch normalization, and ReLU activation functions. Each residual block incorporates a skip connection (or shortcut connection) that directly adds the input of the block to the output of its main path via an addition layer, before passing through a final ReLU

activation. The architecture concludes with a global average pooling layer that reduces the spatial dimensions, followed by a fully connected layer for classification into five classes, and finally, softmax and classification layers. The segmentation results are presented in Table IV. One notices slightly better results for the original 187 band segmentation. We also tested an U-Net architecture (included in Matlab), the results are depicted in Table V.

To enhance the discriminatory power of the previous 1D ResNet architecture, we integrated a Squeeze-and-Excitation (SE) attention mechanism [15] after the residual blocks. Unlike standard 1D CNNs that treat all spectral channels with equal priority, this attention layer adaptively recalibrates channel-wise feature responses by explicitly modeling interdependencies between spectral bands. The SE block 'squeezes' the global spectral information and 'excites' it through a non-linear gating mechanism, allowing the network to focus on the most informative vegetation indices and spectral signatures while suppressing redundant data. This architectural refinement aligns with current state-of-the-art trends in hyperspectral image analysis, moving beyond static feature extraction toward dynamic, attention-driven spectral learning, which is particularly effective for distinguishing crops with high spectral similarity. The results obtained are presented in Table VI.

Although for the last three methods the segmentation accuracy obtained using the reduced set of 27 vegetation indices is slightly lower than that achieved with the full 187-band hyperspectral image, the results remain comparable. Importantly, this approach enables an almost sevenfold reduction in input dimensionality (from 187 to 27), significantly decreasing data redundancy while preserving most of the segmentation performance.

4. Conclusion

In this paper we proposed a methodology for redundancy reduction within a space of 36 selected VIs based on a correlation study. The proposed algorithm for elimination of VIs relies on SSIM computed on the first component of PCA applied on a subset of VIs. The algorithm determines when the resulted reduced subset of VIs has a lower intra-correlation. Our method also takes into account the spatial organization of the information during dimensionality reduction, making it superior to simple statistical methods such as canonical correlation analysis or mutual information. This reduced subset of less-correlated VIs is used as input for a random forest-based segmentation of agricultural crops. The obtained result is compared in terms of accuracy with a random forest segmentation directly applied on the 187-band image. We conclude that similar segmentation accuracy is achieved when using a set of highly relevant vegetation indices selected by the proposed approach, compared to using the entire hyperspectral image data.

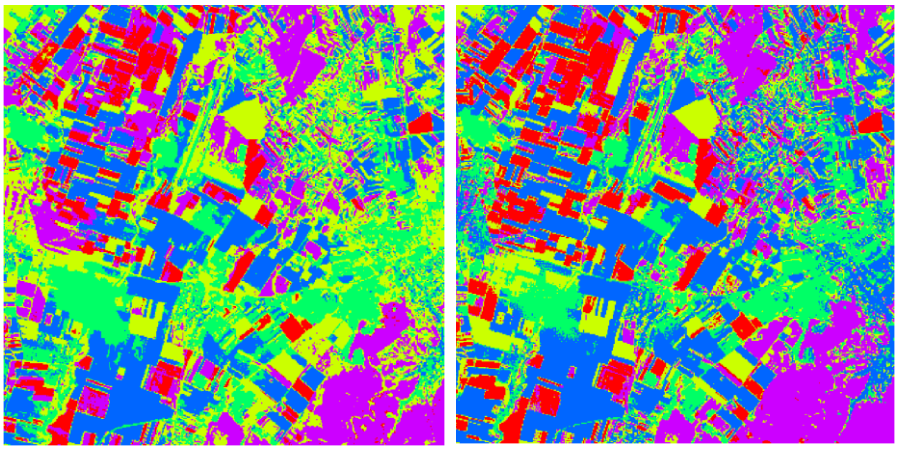

Fig. 6. a) RF segmented image, 5 classes, with input data all the 187 hyperspectral bands. b) RF segmented image, 5 classes, having as input data the 27 VIs.

Table 3

Segmentation Accuracy Assessment (RF)

Segmentation type	**crop type**	**Jacc. (%)**	**RI (%)**	**F1 score (%)**	**BE**
input 187 bands	wheat	0.87	0.99	0.93	0.13
	rapeseed	1.00	1.00	1.00	0.00
input 27 VIs	wheat	**0.91**	0.99	**0.95**	**0.09**
	rapeseed	1.00	1.00	1.00	0.00

Table 4

Segmentation Accuracy Assessment (ResNet)

Segmentation type	**crop type**	**Jacc. (%)**	**RI (%)**	**F1 score (%)**	**BE**
input 187 bands	wheat	0.89	0.99	0.94	0.11
	rapeseed	0.99	1.00	0.99	0.001
input 27 VIs	wheat	0.75	0.99	0.86	0.25
	rapeseed	0.99	1.00	0.99	0.001

Table 5

Segmentation Accuracy Assessment (U-Net)

Segmentation type	**crop type**	**Jacc. (%)**	**RI (%)**	**F1 score (%)**	**BE**
input 187 bands	wheat	0.89	0.99	0.94	0.1
	rapeseed	0.99	1.00	0.99	0.005
input 27 VIs	wheat	0.85	0.99	0.92	0.14
	rapeseed	0.99	1.00	0.99	0.005

Table 6

Segmentation Accuracy Assessment (SE ResNet)

Segmentation type	crop type	Jacc. (%)	RI (%)	F1 score (%)	BE
input 187 bands	wheat	0.89	0.99	0.95	0.1
	rapeseed	0.96	0.99	0.98	0.042
input 27 VIs	wheat	0.76	0.99	0.86	0.24
	rapeseed	0.97	0.99	0.99	0.025

Acknowledgement

This work was partially supported by a grant of the Ministry of Research, Innovation and Digitization, CCDI-UEFISCDI, ELIAC (Early Identification of Agricultural Crops) project no. PN-IV-P7-7.1-PED-2024-0375 in PNCDI IV.

This work was partially funded by the European Union. The AI4AGRI project entitled "Romanian Excellence Center on Artificial Intelligence on Earth Observation Data for Agriculture" received funding from the European Union's Horizon Europe research and innovation program under grant agreement no. 101079136. Views and opinions expressed are however those of the author(s) only and do not necessarily reflect those of the European Union. Neither the European Union nor the granting authority can be held responsible for them.

The authors would like to thank the Italian Space Agency (ASI) for providing the PRISMA images.

R E F E R E N C E S

[1] Billy G. Ram, Peter Oduor, C. Igathinathane, Kirk Howatt, Xin Sun, "A systematic review of hyperspectral imaging in precision agriculture: Analysis of its current state and future prospects," Computers and Electronics in Agriculture, vol. 222, 109037, 2024, doi: 10.1016/j.compag.2024.109037.

[2] Xue, Jinru, Su, Baofeng, "Significant Remote Sensing Vegetation Indices: A Review of Developments and Applications," Journal of Sensors, 1353691, 2017. doi: 10.1155/2017/1353691

[3] E. Boegh, H. Soegaard, N. Broge, C.B. Hasager, N.O. Jensen, K. Schelde et al., „Airborne multispectral data for quantifying leaf area index, nitrogen concentration, and photosynthetic efficiency in agriculture", Rem. Sens. of Env., 81, pp.179−193, 2002

[4] Z. Jiang, A. R. Huete, K. Didan, T. Miura, "Development of a two-band enhanced vegetation index without a blue band", Rem. Sens. of Env., vol. 112, iss. 10, 2008, pp. 3833-3845, doi:10.1016/j.rse.2008.06.006

[5] M. J. Hill, "Vegetation index suites as indicators of vegetation state in grassland and savanna: An analysis with simulated SENTINEL 2 data for a North American transect", Rem. Sens. of Env., vol 137, pp. 94-111, 2013, doi:10.1016/j.rse.2013.06.004

[6] M. Ivanovici, G. Olteanu, C. Florea, RM. Coliban, M. Ștefan, K. Marandskiy, Digital Transformation in Agriculture. In: Ivascu, L., Cioca, LI., Doina, B., Filip, F.G. (eds) Digital Transformation. Intelligent Systems Reference Library, vol 257. Springer, Cham., 2024 doi: 10.1007/978-3-031-63337-9_9

[7] “PRISMA Products Specification Document”, Issue 2.3 Date 12/03/2020, available online at https://prisma.asi.it
[8] A. A. Gitelson and M. N. Merzlyak, “Signature Analysis of Leaf Reflectance Spectra: Algorithm Development for Remote Sensing of Chlorophyll,” Journal of Plant Physiology, vol. 148, Issues 3-4, pp. 494-500, 1996, doi: 10.1016/S0176-1617(96)80284-7.
[9] Z. Wang, A. C. Bovik, H. R. Sheikh and E. P. Simoncelli, "Image quality assessment: from error visibility to structural similarity," IEEE Trans. on Image Proc., vol. 13, no. 4, pp. 600-612, 2004, doi: 10.1109/TIP.2003.819861.
[10] L. Breiman, "Random Forests." Machine Learning, vol. 45, pp. 5-32, 2001, doi: 10.1023/A:1010933404324.
[11] S. Zambanini, R. Sablatnig, H. Maier and G. Langs, "Automatic imagebased assessment of lesion development during hemangioma follow-up examinations”, Artif. Intell. in Med., vol. 50, iss. 2, pp. 83–94, 2010, doi: 10.1016/j.artmed.2010.06.003.
[12] D. Hong et al., "SpectralFormer: Rethinking Hyperspectral Image Classification With Transformers," in IEEE Transactions on Geoscience and Remote Sensing, vol. 60, pp. 1-15, 2022, Art no. 5518615, doi: 10.1109/TGRS.2021.3130716.
[13] L. Sun, G. Zhao, Y. Zheng and Z. Wu, "Spectral–Spatial Feature Tokenization Transformer for Hyperspectral Image Classification," in IEEE Transactions on Geoscience and Remote Sensing, vol. 60, pp. 1-14, 2022, Art no. 5522214, doi: 10.1109/TGRS.2022.3144158.
[14] M. Ahmad, M. Mazzara, S. Distefano, A. M. Khan and S. L. Ullo, "DiffFormer: A Differential Spatial-Spectral Transformer for Hyperspectral Image Classification," in IEEE Journal of Selected Topics in Applied Earth Observations and Remote Sensing, vol. 18, pp. 10419-10428, 2025, doi: 10.1109/JSTARS.2025.3558889.
[15] J. Hu, L. Shen and G. Sun, "Squeeze-and-Excitation Networks," 2018 IEEE/CVF Conference on Computer Vision and Pattern Recognition, Salt Lake City, UT, USA, 2018, pp. 7132-7141, doi: 10.1109/CVPR.2018.00745.